ANALYSIS OF ADHESIVE PENETRATION INTO WOOD USING NANO-X-RAY COMPUTED TOMOGRAPHY

*Paige McKinley**†
Graduate Research Assistant
E-mail: paigemckinley@bc.com

Frederick A. Kamke†
Professor
E-mail: fred.kamke@oregonstate.edu

Arijit Sinha†
Associate Professor
Department of Wood Science & Engineering
Oregon State University
Corvallis, OR 97331
E-mail: arijit.sinha@oregonstate.edu

Vincent De Andrade
Beamline Scientist
X-ray Division
Advanced Photon Source
Argonne National Laboratory
Lemont, IL 60439
E-mail: vdeandrade@aps.anl.gov

Joseph E. Jakes†
Research Materials Engineer
Forest Biopolymers Science and Engineering
USDA Forest Service
Forest Products Laboratory
Madison, WI 53726

(Received July 2017)

Abstract. This study focused on the penetration of adhesive into cell lumens and cell walls. Douglas-fir samples containing an iodinated phenol-formaldehyde adhesive were analyzed using nano-X-ray computed tomography (XCT), X-ray fluorescence microscopy, and energy-dispersive X-ray spectroscopy to observe adhesive penetration in cell walls. A gradient of penetration was observed within the cell wall structure. In addition, these nano-XCT datasets were indexed to previous micro-XCT datasets, which gave the ability to link the nanoscale cell wall penetration to microscale penetration in to the porous network of cell lumens.

Keywords: Nano-X-ray computed tomography, X-ray fluorescence microscopy, energy-dispersive X-ray spectroscopy, adhesive, cell wall penetration.

INTRODUCTION

It has been hypothesized that the performance of wood-adhesive bondlines subjected to stresses will depend on the micro- and nanoscale interactions of the wood and adhesive in the bonded interphase. There are two forms of adhesive penetration—gross penetration and cell wall penetration. Gross penetration is easily achievable and refers to the adhesive flowing into the porous wood structure (cell lumens, pits,

* Corresponding author
† SWST member

intercellular voids, and cracks). This is essential for creating a sound bond because the adhesive fills voids, creates additional surface contact, and promotes mechanical interlocking. Cell wall penetration refers to infiltration of the adhesive into the cell wall substance before polymerization. It has been proposed that cell wall penetration can reinforce the cells and create a bond that will be more resistant to shrinkage/swelling due to the mixed properties of wood substance and adhesive. This can be particularly beneficial for improving water resistance and can potentially transfer stresses more efficiently from one substrate to the other. Cell wall penetration may be particularly beneficial for improving water resistance because adhesive polymers may block pathways for water infiltration or preswell the cell wall, thus reducing swelling potential on exposure to water.

Measuring adhesive penetration into the wood cell wall is not a trivial task attributable to the scale and chemical similarity between common industrial adhesives and the wood cell wall. Analytical methods, such as differential X-ray diffraction, that identify atomic element concentration in the cell wall cannot differentiate between carbon and oxygen content originating from the cell wall vs the same element present in phenol-formaldehyde (PF). Ultraviolet microscopy (Gindl 2001; Gindl et al 2002), nanoindentation (Gindl et al 2004; Stöckel et al 2012), and X-ray fluorescence microscopy (XFM) (Jakes et al 2015) experiments have successfully detected adhesive in the cell wall molecular structure. These methods require damaging the specimen to obtain a clean section or surface and only provide information about the 2D surface that is exposed for examination. The 3D view of the wood-adhesive interaction provides a measure of volume, and thus an opportunity to observe pathways for adhesive penetration into wood.

To accurately assess the anatomical features in biological materials at the micron scale, X-ray computed tomography (XCT) has been successfully used to visualize the complex structure of natural materials (Steppe et al 2004; Trtik et al 2007; Mannes et al 2010; Mayo et al 2010; Standfest et al 2010; Hass et al 2012; Zauner et al 2012; Kamke et al 2014; Paris and Kamke 2015; McKinley et al 2016). XCT is a high-resolution, 3D, nondestructive method to analyze materials and potentially segment material phases within a dataset (Metscher 2013). Previous studies have successfully scanned and segmented material phases within wood-adhesive samples using micro-XCT (Evans et al 2010; Modzel et al 2011; Paris et al 2014), which provides spatial resolution to approximately 1 μm. To gain further information regarding penetration of adhesive into pits and cell walls, nano-XCT (<100 nm) must be achieved. Although gaining resolution, the sample size must be reduced, resulting in sample preparation complications and a reduced scan region. Nano-XCT has been successful in visualizing samples, such as mouse bone (Schneider et al 2007; Khoury et al 2015), electrodes in a battery (Létiche et al 2017; Lim et al 2016), or fuel cell (Shearing et al 2011; Cetinbas et al 2017), and the pore structure of tight sandstone from reservoirs (Bin et al 2013). The present research was the first to apply nano-XCT methodology to the wood-adhesive interphase.

MATERIALS AND METHODS

Douglas-fir (*Pseudotsuga menziesii*) sapwood at 12% MC was used for this study. Solid sawn samples were cut to 64 mm 100 mm 6 mm (T L R), freshly planed, and parallel bonded with a PF adhesive tagged with iodine. The iodine tag was needed to create X-ray attenuation contrast between the adhesive and cell wall substance. Details on the adhesive formulations and sample preparation were previously reported (Paris et al 2014). The nano-XCT samples discussed in this article were bonded with iodinated PF (I-PF). All phenol used to formulate the PF resin was iodophenol. To insure that iodine did not separate from the PF and independently migrate into the wood, ion chromatography and energy-dispersive spectroscopy were used to analyze the liquid resin and cured bondlines, respectively. Results confirmed that any iodine detected in the sample was associated with PF resin (Paris et al 2014). To achieve

potential differences in penetration, high and low-molecular-weight PF were prepared. The high-molecular-weight PF was achieved by extending the time of the resin cook procedure. Gel permeation and ion chromatography analyses were used to measure the molecular weight and polydispersity of each adhesive. The high-molecular-weight PF for this study had a weight average molecular weight of 28,050 g/mol and a polydispersity index of 1.135. The low-molecular-weight PF was formulated with a weight average molecular weight of 18,110 g/mol and a polydispersity index of 1.097 (Paris et al 2014). Both PF formulations have a broad distribution of molecular weight. It is assumed that only the low end of the distribution is capable of penetrating the cell wall.

Nano-XCT Sample Preparation

Nano-XCT samples were cut from previously scanned micro-XCT samples. The micro-XCT samples were scanned at the Advanced Photon Source (APS), Argonne National Laboratory, on the 2 bending magnet (BM) beamline, with a resolution of 1.3 μm^3/voxel. The micro-XCT datasets were used to locate areas within the sample that appeared to have adhesive penetration into the cell wall. Only scans from earlywood cells are reported because the latewood scans had insufficient quality in the reconstructed images. These sub-datasets were indexed and compared with the physical micro-XCT sample. The area of interest (AOI) within the physical sample was located using anatomical features observed on the surface using an epifluorescence microscope. This became the AOI for the nano-XCT study.

The AOI was excised from the micro-XCT samples using a hand-held razorblade and a stereo microscope. The nano-XCT sample dimensions were approximately 40 μm 40 μm 120 μm. The nano-XCT samples were then mounted on the tip of a metal pin (sewing needle) with quick-setting epoxy (Clear Weld; JB Weld Company, Sulphur Springs, TX). The mounting procedure began by placing the sample flat on a glass slide. The extreme tip of the metal pin was dipped in epoxy and then held upside down for 3 min so that the epoxy partially cured. Using forceps, the epoxy on the tip of the pin was gently placed in contact with the specimen. The vertical alignment of the sample on the pin was crucial so that the sample stayed within the 50 μm 50 μm field of view (FOV) of the XCT beamline. With the sample attached, the pin was held upside down until the epoxy fully cured (Fig 1, right). Each specimen was carefully identified and the orientation was indexed from the original micro-XCT sample for reference after nano-XCT scanning. The pin was then mounted on the nano-XCT sample holder (Fig 1, left).

Nano-XCT Scanning at the APS

The samples were scanned at the APS on beamline 32 insertion device (ID) using a full-field transmission X-ray microscope (De Andrade et al 2016). The scanning parameters are listed in Table 1. To prevent shrinking and swelling attributable to moisture sorption, the samples were allowed to equilibrate to the laboratory conditions overnight. During scanning, sample movement will corrupt the image reconstruction as computed tomography algorithms require the reconstructed object to stay perfectly immobile in respect to the rotating plate referential. The first set of specimens experienced movement during the scans. A second attempt encapsulated the sample inside a polyimide (Kapton®) capillary tube, which was sealed with epoxy, but

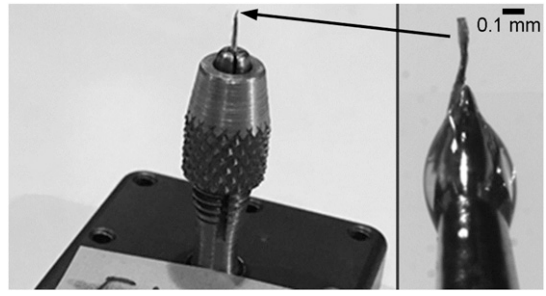

Figure 1. Nano-X-ray computed tomography specimen held in a microchuck on the left; sample mounted on the top of the pin with epoxy on the right.

Table 1. Scanning parameters for nano-X-ray computed tomography samples on Advanced Photon Source beamline 32ID.

Beam energy (KeV)	8	
Exposure time (ms)	500	
Scan time (min)	10	
Number of projections	361	
Step size (°)	2	
Distance to scintillator film (m)	3	
Voxel size (nm^3)	60	
Field of view (μm)	100	100

movement still occurred because of radiation damage that is common on soft tissues. These damages caused a slow rotation as the microstructure unwound. Subsequently, a "precooking" procedure was used. The remaining specimens were exposed to the X-ray beam and rotated for 20 min, before capturing the XCT data. The 20-min beam exposure allowed the deformation to dissipate. In addition, the number of projections was reduced to 361, thus reducing the total time of exposure. Comparison of radiograms before and after the precooking procedure showed very little movement. The measured 2D spatial resolution, using a 30-nm Siemens star as a reference, was 60 nm. The voxel size of the 3D reconstructions was 60 60 60 nm^3.

Image reconstruction was performed using algorithms prepared by the APS and implemented in TomoPy (De Carlo et al 2014; Gürsoy et al 2014; Miqueles et al 2014; Pelt and Batenburg 2015).

Adhesive Penetration in Cell Walls

The resulting tomograms were analyzed using the image analysis software package FIJI (Schindelin et al 2012), in particular the 3D Analyzer plug-in and the orthogonal view tools. Even with the efforts to reduce sample movement, only three datasets were of adequate quality to use for adhesive penetration analysis. All of the usable datasets were bonded with the low-molecular-weight I-PF; therefore, a comparison of adhesive penetration into the cell wall based on molecular weight could not be completed. Despite the difference in the FOV (2 2 2 mm^3 vs 0.05 0.05 0.05 mm^3), bordered pits, ray cells, and detailed preanalysis note-taking allowed for successful identification of the nano-XCT samples within the micro-XCT dataset.

Measurement of adhesive penetration into the cell wall was based on voxel grayscale value of the reconstructed images. The reconstructed 32-bit image stacks were examined to find cell lumens that were filled with adhesive and free from voids and XCT scanning artifacts. A cross-section view was chosen, and the analysis was performed on an individual slice (thickness of one voxel) within the stack. An AOI was then defined by a rectangle that was five voxels wide and length of various dimensions depending on the sample. The AOI was oriented such that width (y-coordinate) was parallel to the cell wall and the length (x-coordinate) extended through the cell wall. A grayscale profile plot was then created, where the average grayscale value of the five voxels in the y-direction was calculated and then plotted as a function of the x-coordinate. The assumption was that increasing grayscale value corresponds to increasing adhesive concentration. The analysis was performed on different cell walls and on different regions of the same cell wall. The selection of five voxels for the width of the AOI reduced the influence of cell wall curvature. X-ray diffraction did not appear to be an issue at the interface between the cell wall and the adhesive-filled lumen. Nevertheless, complementary analysis techniques were conducted for comparison.

XFM was performed at the APS on beamline 2ID-E. A full description of how XFM can be used to map adhesive penetration into wood cell walls was reported by Jakes et al (2015), and similar procedures were used in this work. Bonded samples containing the high-molecular-weight I-PF were used. These samples had been previously scanned with micro-XCT. A 2-μm-thick cross section of the bondline was cut dry with a diamond knife fit into a Leica EM UC7 ultramicrotome (Wetzlar, Germany). The section was secured and held flat between two Norcada 200-nm-thick silicon nitride windows (Edmonton, AB, Canada). The incident X-ray beam was

focused to a spot approximately 0.5 μm in diameter at full width at half maximum. The beam energy was 10.2 keV. XFM elemental maps of iodine were built by raster-scanning imaging, using 0.3-μm step sizes with 5-ms dwell times at each step. XFM data analysis was performed using MAPS software (Vogt 2003). In brief, the full spectra were fit to modified Gaussian peaks, the background was iteratively calculated and subtracted, and the results were compared with standard reference materials (RF8-200-S2453; AXO GmbH, Dresden). Image analysis was carried out using FIJI (Schindelin et al 2012), and 32-bit tiff images were exported from the MAPS software. A Gaussian blur (sigma (radius) = 1) filter was applied to the XFM map. Measurement of adhesive penetration into the cell wall was based on measured iodine intensity. An intensity profile across a cell wall was measured from the XFM iodine map using an AOI defined by a rectangle that was 5 pixels wide.

The I-PF-bonded samples were also examined by scanning electron microscopy (SEM), along with energy-dispersive X-ray spectroscopy (EDS). Areas within the sample that had lumens filled with adhesive were selected. EDS line mapping was then used to detect relative concentration of iodine in the cell wall. Because iodine was covalently bonded to all phenol groups in the PF resin, the presence of iodine confirmed the presence of PF resin.

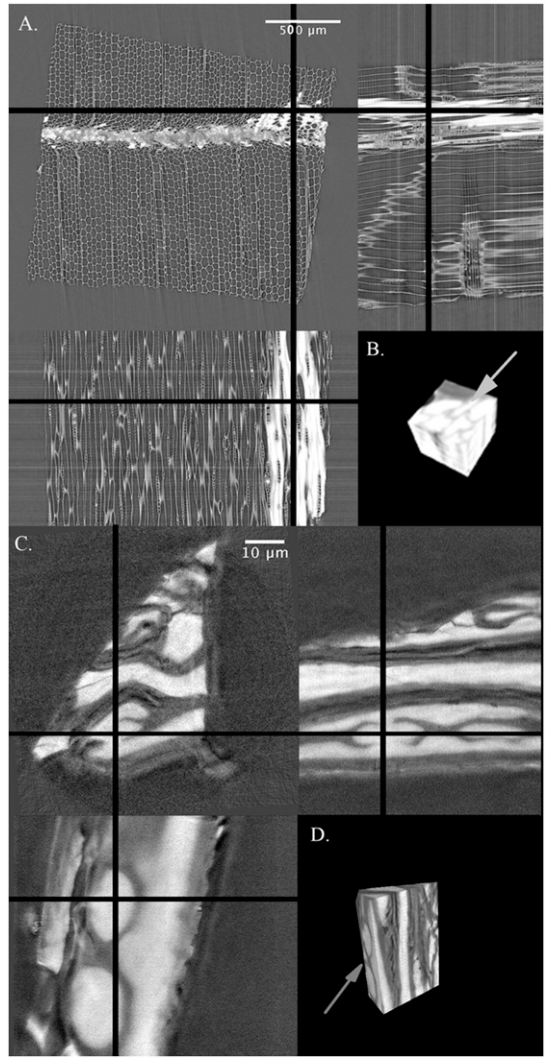

Figure 2. Locating nano-X-ray computed tomography (XCT) specimen within the micro-XCT dataset; (a) original micro-XCT dataset with crosshairs and orthogonal views showing the location of the nano-XCT sample; (b) 3D view of the location within the micro-XCT dataset with the arrow emphasizing the elongated, crushed, earlywood cell in the nano-XCT sample; (c) the nano-XCT sample with orthogonal views showing bordered pits filled with adhesive; (d) 3D view of the nano-XCT sample with the arrow emphasizing bordered pits; right corner of 3D view shows crushed ray lumens.

RESULTS AND DISCUSSION

The nano-XCT specimen was identified within the master micro-XCT dataset for all three datasets (Figs 2 and 3). Some aspects of the nano-XCT sample preparation could have been improved. The micro-XCT samples did not contain a point of reference within the dataset to match with the physical sample. A fiducial marker would have saved time when matching the micro-XCT dataset to the sample to locate the AOI.

With the exception of ring removal during image reconstruction, the nano-XCT image slices were not processed, and the 32-bit images were used for the final analysis. At 60 60 60 nm^3/voxel, every adhesive molecule cannot be distinguished. However, with double cell wall thickness in the

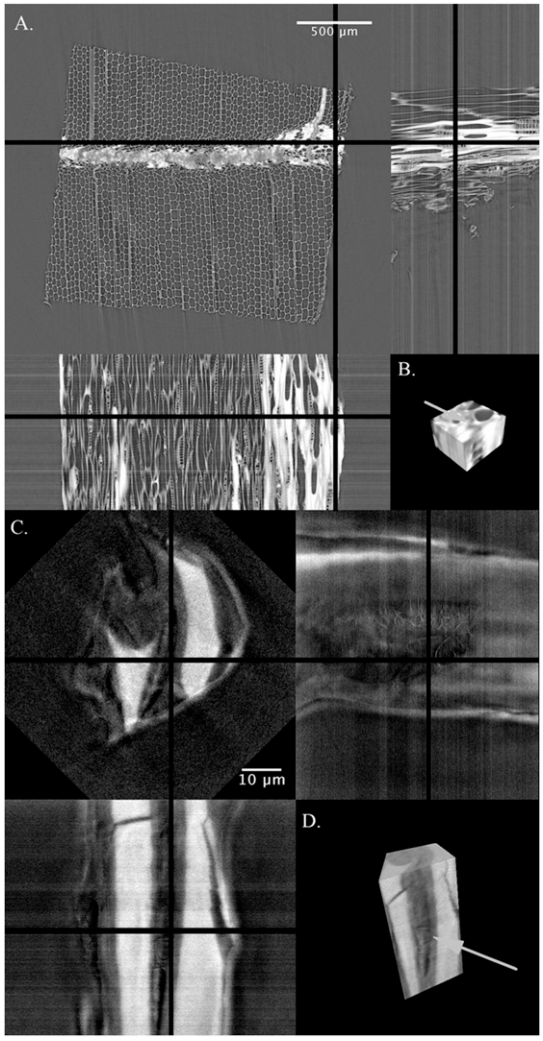

Figure 3. Locating the nano-X-ray computed tomography (XCT) specimen within the master micro-XCT dataset; this sample is located 40 µm above the nano-XCT sample in Fig. 2; (a) original micro-XCT dataset with crosshairs and orthogonal views showing location of the nano-XCT sample; (b) 3D view of location within micro-XCT dataset with arrow emphasizing the crushed ray; (c) the nano-XCT sample rotated CW 315° with orthogonal views showing voids in crushed ray and complex microstructure of the cell wall; (d) 3D view of the nano-XCT sample with the arrow emphasizing the end of crushed rays on side between two cell lumens filled with adhesive.

earlywood region of 2-4 µm, a gradient can be detected. Figures 4–6 illustrate the gradient in grayscale in the cell wall, which is proposed to be associated with a gradient of adhesive penetration. If no adhesive penetration was present, the difference in grayscale values would be abrupt, resulting in a vertical line in the grayscale profile at the surface of the lumen. Other grayscale profiles were created between adhesive and void, and cell wall and void, resulting in an abrupt transition of 3-4 voxels. Adhesive penetration into the cell wall varied between 0.8 µm (Fig 3) and 2.5 µm (Fig 5), which corresponded to 13 and 42 voxels, respectively.

In the micro-XCT datasets, it was noticed that the compound middle lamella (CML) had a higher X-ray attenuation value than the rest of the cell wall. For the micro-XCT study, this did not hinder the analysis; however, on the nano scale, the distinction between adhesive and cell wall is more critical. Because the CML is rich in lignin, a delignification treatment using peracetic acid was attempted, but the resulting samples were too fragile, and the adhesive was degraded from the acid. These samples were not used in the analysis.

Some datasets showed a gradient in X-ray attenuation in lumens filled with adhesive, in the region adjacent to the cell wall (Fig 6). Because all phenol was covalently bonded to iodine, this observation may be caused by lower density of the cured PF near the cell wall. Similar behavior was found in analyses using XFM and EDS. One cannot rule out the possibility of X-ray diffraction causing a gradient of grayscale at the interface of adhesive and cell wall, but XFM and EDS results are consistent with grayscale profile. Previous research supports some inhomogeneity of PF in the close proximity of the cell wall. A report by Jeremic et al (2007) describes an EDS experiment measuring penetration of bromine-tagged PEG into wood cell walls. Microtomed specimens (0.2 µm thick) were embedded with Spurr's resin containing epichlorohydrin-polyglycol, which contains chlorine. The subsequent EDS scans revealed a low concentration of chlorine within a region of 1 µm of the cell wall. According to the authors, this was due to the separation of the embedding media from the cell wall. Yet visual

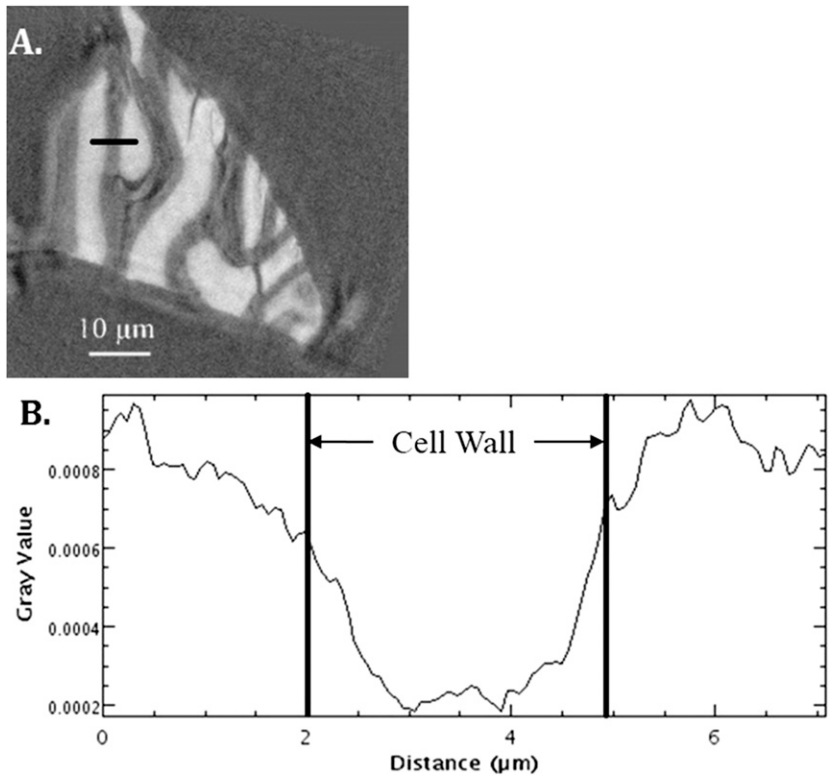

Figure 4. Adhesive penetration analysis of the nano-X-ray computed tomography (XCT) sample in Fig. 2; (a) nano-XCT cross-sectional grayscale slice; line indicates box scan; (b) grayscale box analysis across line in (a); vertical lines represent the location of cell wall edges.

inspection of the SEM images in the region of the EDS line scan showed no evidence of separation. Xu et al (2016) demonstrated a gradient in PF concentration close to the cell wall using scanning thermal microscopy. The authors made no comment on the cause of the gradient, but the results showed a region of approximately 1 µm within a PF-filled lumen where the signal was consistent with a lower PF concentration.

Figure 7 shows an example of an EDS line scan for iodine in the region of an adhesive-filled lumen. The high-molecular-weight I-PF is shown in Fig 7(a) and the low-molecular-weight I-PF is shown in Fig 7(b). The relative net intensity of iodine is overlaid on the SEM image. The light areas are adhesive, gray areas are cell wall, and black area is void. The black line indicates the scan line. In Fig 7(a), at the left is cell wall, then progressing to the right is void, adhesive in lumen, double cell wall, adhesive in lumen, and cell wall. There is clear evidence of an iodine gradient in the adhesive-filled lumens. Iodine in the cell wall, if present, is near the detection limit. Figure 7(b) shows an adhesive-filled lumen at left, then progressing to the right is a double cell wall and another adhesive-filled lumen. The iodine line scan shows evidence that iodine associated with the low-molecular-weight I-PF is in the cell wall. A gradient of iodine in the adhesive-filled lumens is also shown. EDS results indicate detection of iodine in the cell wall at a depth of 0.5-1 µm.

An XFM iodine map is shown in Fig 8(a) for the high-molecular-weight I-PF in a sample of Douglas-fir latewood. No XFM analysis was performed on the low-molecular-weight I-PF. The white areas are regions of high iodine

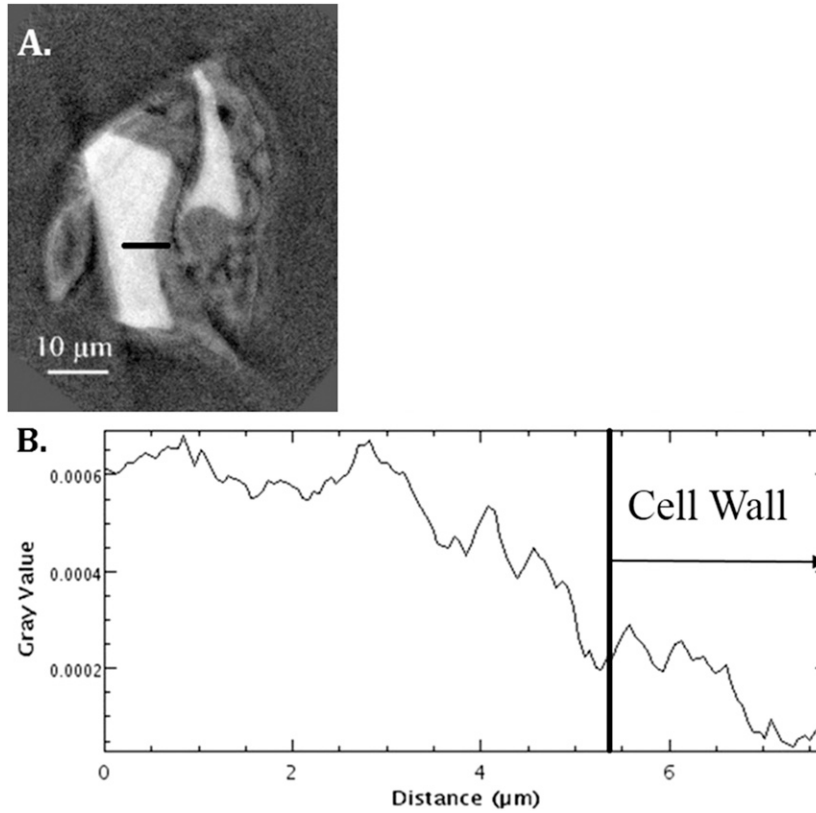

Figure 5. Adhesive penetration analysis of the nano-X-ray computed tomography (XCT) sample in Fig. 3; (a) nano-XCT cross-sectional grayscale slice; the line indicates box scan; (b) grayscale box analysis across line in (a); the vertical line represents the location of cell wall edge.

concentration, where black areas have no detectable iodine. The iodine intensity is directly proportional to the amount of adhesive, and the gray color of the cell walls in the iodine XFM map definitively shows that adhesive penetrates into the cell walls. However, an adhesive gradient is less straightforward to observe because the distribution of X-rays in the focused spot can cause distortions that look like gradients, especially near sharp interfaces with a strongly fluorescing material such as I-PF. To determine whether an adhesive gradient existed in the wood cell walls, a tracheid with a partially filled lumen was chosen for further analysis (inset of Fig 8b). This partially filled tracheid was in a different region of the same section shown in Fig 8(a). The concentration profiles in Fig 8(b) compare the gradients across the I-PF–empty lumen interface and the I-PF–cell wall interface. We assume the I-PF–empty lumen interface is sharp, and the observed gradient at this interface is a result of the distribution of X-rays in the focused spot. Comparing the two profiles shows that most of the gradient at the cell wall interface arises from the sharp edge of the I-PF at this interface. However, as an approximation, the cell wall gradient can be corrected by subtracting the gradient at the empty lumen interface from the gradient at the cell wall interface. In Fig 8(c), the corrected gradient of iodine intensity inside the cell wall is plotted, revealing a gradient with the iodine intensity decreasing from about 1.5 to 4 µm into the cell wall. An uncertainty in the corrected gradient is the proper alignment in the distance of the empty lumen and cell wall gradients. However,

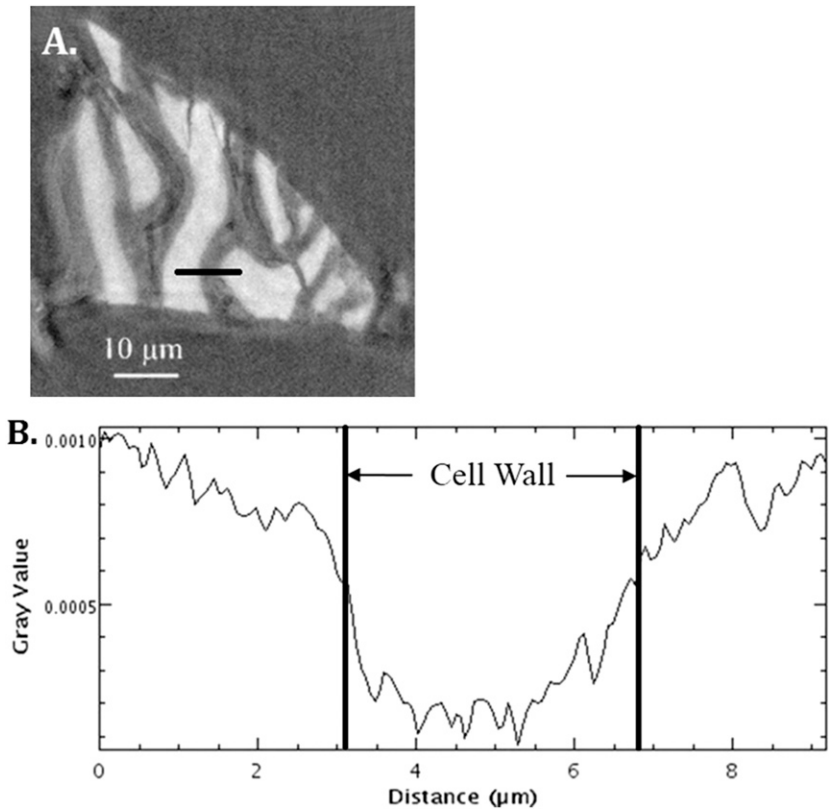

Figure 6. Adhesive penetration analysis of the nano-X-ray computed tomography (XCT) sample in Fig. 2; (a) original nano-XCT cross-sectional grayscale slice with pink line indicating box scan; (b) grayscale box analysis across line in (a); vertical lines represent the location of cell wall edges.

the observed gradient in iodine from 1.5 to 4 μm into the cell wall can be observed even if the interface locations are misaligned by 0.2 μm (data not shown). To observe adhesive gradients closer than 1.5 μm from the interface, either a more detailed analysis would be needed or imaging performed with an X-ray beam focused to a smaller probe size.

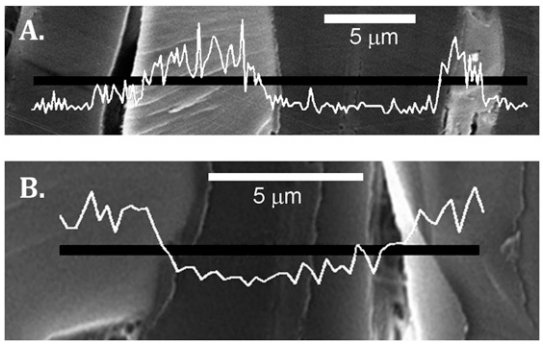

Figure 7. Energy-dispersive X-ray spectroscopy line scan for iodine in sample bonded with high-molecular-weight iodinated phenol-formaldehyde (I-PF) (a) and low-molecular-weight I-PF (b).

CONCLUSIONS

Nano-XCT was employed to observe features in a wood-adhesive bondline using a spatial resolution of 60 nm. Companion analysis using micro-XCT permitted locating the nano-XCT sample within the micro-XCT sample. The FOV of the nano-XCT datasets was 50 μm 50 μm 50 μm, which permitted only 1-2 Douglas-fir cells to be observed. Sample movement during the XCT scan was difficult to control. Some successful scans were obtained by

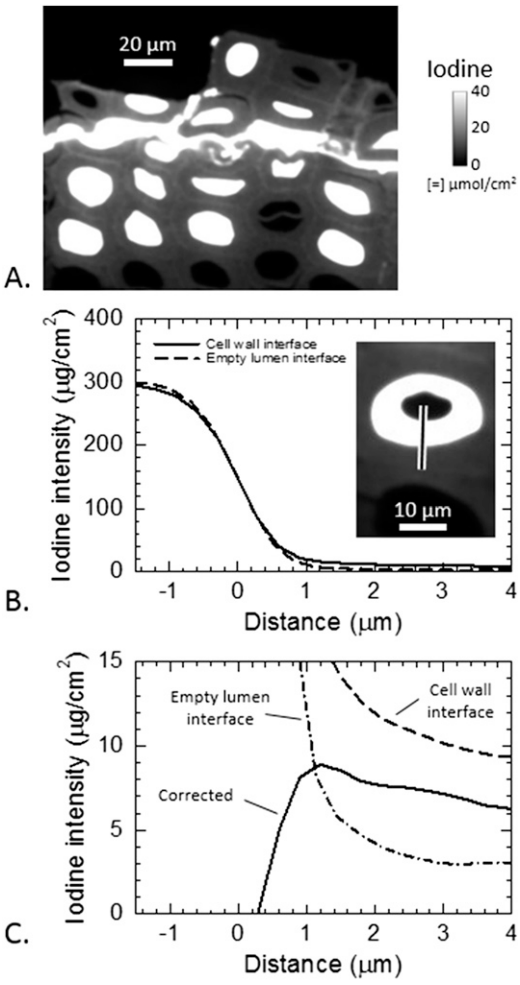

Figure 8. X-ray fluorescence microscopy mapping of high-molecular-weight iodinated phenol-formaldehyde (I-PF) adhesive in a wood-adhesive bondline; (a) Iodine map showing I-PF in bondline; (b, inset) Iodine map of a partially filled lumen with an area of interest showing where the intensity profiles were taken. From the top to the bottom, the line goes from the empty part of the lumen, to the I-PF coating the lumen surface, to the cell wall. (b) Iodine intensity profile plots across the I-PF–cell wall and I-PF–empty lumen interfaces. The distances in the profile plots were defined such that the I-PF was at negative values, and the middle of the gradient was used to define 0. The positive distances are either cell wall or air. (c) Profile plots of the empty lumen interface, cell wall interface, and corrected gradient. The corrected gradient is the difference between the cell wall interface and empty lumen interface gradients.

pretreating the sample with the X-ray beam before data collection. Using XCT at a resolution of 60 nm^3/voxel, evidence of penetration for the low-molecular-weight I-PF adhesive into the cell wall was obtained. Complimentary analysis using EDS and XFM revealed a similar penetration depth of 0.5-1 µm. With improvements on sample preparation, scanning conditions, and image reconstruction, future nano-XCT studies may yield more usable datasets.

ACKNOWLEDGMENTS

This research used resources of the Advanced Photon Source, a U.S. Department of Energy (DOE) Office of Science User Facility operated for the DOE Office of Science by the Argonne National Laboratory under Contract No. DE-AC02-06CH11357. Financial support was received from U.S. National Science Foundation Grant No. IIP-1331043, and the NSF Industry/University Cooperative Research Center for Wood-Based Composites Grant No. IIP-1034975.

REFERENCES

Bin B, Rukai Z, Songtao W, Wenjing Y, Gelb J, Gu A, Xiangxiang Z, Ling S (2013) Multi-scale method of nano(micro)-CT study on microscopic pore structure of tight sandstone of Yanchang Formation, Ordos Basin. Petrol Explor Dev 40(3):354-358.

Cetinbas FC, Ahluwalia RK, Kariuki N, De Andrade V, Fongalland D, Smith L, Sharman J, Ferreira P, Rasouli S, Myers DJ (2017) Hybrid approach combining multiple characterization techniques and simulations for microstructural analysis of proton exchange membrane fuel cell electrodes. J Power Sources 344:62-73.

De Andrade V, Deriy A, Wojcik MJ, Gürsoy D, Shu D, Fezzaa K, De Carlo F (2016) Nanoscale 3D imaging at the advanced photon source. SPIE Newsroom May 12, 2016. doi: 10.1117/2.1201604.006461.

De Carlo F, Gursoy D, Marone F, Rivers M, Parkinson YD, Khan F, Schwarz N, Vine DJ, Vogt S, Gleber SC, Narayanan S, Newville M, Lanzirotti T, Sun Y, Hong YP, Jacobsen C (2014) Scientific data exchange: A schema for hdf5-based storage of raw and analyzed data. J Synchrotron Radiat 21(6): 1224-1230.

Evans PD, Morrison O, Senden TJ, Vollmer S, Roberts RJ, Limaye A, Arns CH, Averdunk H, Lowe A, Knackstedt MA (2010) Visualization and numerical analysis of adhesive distribution in particleboard using X-ray microcomputed tomography. Int J Adhes Adhes 30:754-762.

Gindl W (2001) SEM and UV-microscopic investigation of glue lines in Parallam PSL. Holz Roh Werkst 59:211-214.

Gindl W, Dessipri E, Wimmer R (2002) Using UV-microscopy to study diffusion of melamine-urea-formaldehyde resin in cell walls of spruce wood. Holzforschung 56:103-107.

Gindl W, Schoberl T, Jeronimidis G (2004) The interphase in phenol-formaldehyde and polymeric methylene di-phenyl-di-isocyanate glue lines in wood. Int J Adhes Adhes 24:279-286.

Gürsoy D, De Carlo F, Xiao X, Jacobsen C (2014) TomoPy: A framework for the analysis of synchrotron tomographic data. J Synchrotron Radiat 21:1188-1193.

Hass P, Wittel FK, Mendoza M, Herrmann HJ, Niemz P (2012) Adhesive penetration in beech wood: experiments. Wood Sci Technol 46:243-256

Jakes J, Hunt C, Yelle D, Lorenz L, Hirth K, Gleber S-C, Vogt S, Grigsby W, Frihart C (2015) Synchrotron-based X-ray fluorescence microscopy in conjunction with nanoindentation to study molecular-scale interactions of phenol-formaldehyde in wood cell walls. ACS Appl Mater Interfaces 7:6584-6589.

Jeremic D, Cooper P, Brodersen P (2007) Penetration of poly (ethylene glycol) into wood cell walls of red pine. Holzforschung 61:272-278.

Kamke FA, Nairn JA, Muszynski L, Paris J, Schwarzkopf M, Xiao X (2014) Methodology for micro-mechanical analysis of wood-adhesive bonds using XCT and numerical modeling. Wood Fiber Sci 46(1):15-28.

Khoury BM, Bigelow EM, Smith L, Schlecht SH, Scheller EL, Andarawis-Puri N, Jepsen KJ (2015) The use of nano-computed tomography to enhance musculoskeletal research. Connect Tissue Res 56(2):106-119.

Létiche M, Eustache E, Freixas J, Demortière A, De Andrade V, Morgenroth L, Tilmant P, Vaurette F, Troadec D, Roussel P, Brousse T, Lethien C (2017) Atomic layer deposition of functional layers for on chip 3D Li-ion all solid state microbattery. Adv Energy Mater 017;7:1601402.

Lim C, Yan B, Kang H, Song Z, Lee WC, De Andrade V, De Carlo F, Yin L, Kim Y, Zhu L (2016) Analysis of geometric and electrochemical characteristics of lithium cobalt oxide electrode with different packing densities. J Power Sources 328:46-55.

Mannes D, Marone F, Lehmann E, Stampanoni M, Niemz P (2010) Application areas of synchrotron radiation tomographic microscopy for wood research. Wood Sci Technol 44:67-84.

Mayo SC, Chen F, Evans R (2010) Micron-scale 3D imaging of wood and plant microstructure using high-resolution x-ray phase-contrast microtomography. J Struct Biol 171:182-188.

McKinley PE, Ching DJ, Kamke FA, Zauner M, Xiao X (2016) Micro X-ray computed tomography of adhesive bonds in wood. Wood Fiber Sci 48:2-16.

Metscher BD (2013) Biological applications of X-ray microtomography: Imaging microanatomy, molecular expression and organismal diversity. Microsc Anal (Am Ed) 27(2):13-16.

Miqueles EX, Rinkel J, O'Dowd F, Bermúdez JSV (2014) Generalized Titarenko's algorithm for ring artefacts reduction. J Synchrotron Radiat 21(6):1333-1346.

Modzel G, Kamke FA, De Carlo F (2011) Comparative analysis of a wood-adhesive bondline. Wood Sci Technol 45:147-158.

Paris J, Kamke F (2015) Quantitative wood-adhesive penetration with X-ray computed tomography. Int J Adhes Adhes 61:71-80.

Paris J, Kamke FA, Mbachu R, Gibson S (2014) Phenol formaldehyde adhesives formulated for advanced X-ray imaging in wood-composite bondlines. J Mater Sci 42(2):580-591.

Pelt DM, Batenburg KJ (2015) Accurately approximating algebraic tomographic reconstruction by filtered back-projection. Pages 158–161 *in* Proc. 2015 International Meeting on Fully Three-Dimensional Image Reconstruction in Radiology and Nuclear Medicine.

Schindelin J, Arganda-Carreras I, Frise E, Kaynig V, Longair M, Pietzsch T, Preibisch S, Rueden C, Saalfeld S, Schmid B, Tinevez J-Y, White DJ, Hartenstein V, Eliceiri K, Tomancak P, Cardona A (2012) Fiji: An open-source platform for biological-image analysis. Nat Methods 9(7):676-682.

Schneider P, Stauber M, Voide R, Stampanoni M, Donahue LR, Müller R (2007) Ultrastructural properties in cortical bone vary greatly in two inbred strains of mice as assessed by synchrotron light based micro- and nano-CT. J Bone Miner Res 22(10):1557-1569.

Shearing PR, Bradley RS, Gelb J, Lee SN, Atkinson A, Withers PJ, Brandon NP (2011) Using synchrotron X-ray nano-CT to characterize SOFC electrode microstructures in three-dimensions at operating temperature. Electrochem Solid-State Lett 14(10):B117-B120.

Standfest G, Kranzer S, Petutschnigg A, Dunky M (2010) Determination of the microstructure of an adhesive-bonded medium density fiberboard (MDF) using 3-D sub-micrometer computer tomography. J Adhes Sci Technol 24:1501-1514.

Steppe K, Cnudde V, Girard C, Lemeur R, Cnudde J-P, Jacobs P (2004) Use of X-ray computed microtomography for non-invasive determination of wood anatomical characteristics. J Struct Biol 148:11-21.

Stöckel F, Konnerth J, Moser J, Kantner W, Gindl-Altmutter W (2012) Micromechanical properties of the interphase in pMDI and UF bond lines. Wood Sci Technol 46:611-620.

Trtik P, Dual J, Keunecke D, Mannes D, Niemz P, Stähli P, Stampanoni M (2007) 3D imaging of microstructure of spruce wood. J Struct Biol 159:46-55.

Vogt S (2003) MAPS: A set of software tools for analysis and visualization of 3D X-ray fluorescence data sets. J Phys IV 104:635-638.

Xu D, Zhang Y, Zhou H, Meng Y, Wang S (2016) Characterization of adhesive penetration in wood bond by means of scanning thermal microscopy (SThM). Holzforschung 70(4):323-330.

Zauner M, Keunecke D, Mokso R, Stampanoni M, Niemz P (2012) Synchrotron-based tomographic microscopy (SbTM) of wood: Development of a testing device and observation of plastic deformation of uniaxially compressed Norway spruce samples. Holzforschung 66(8): 973-979.